

Using cosmic variance to constrain the dark matter halo mass of Lyman-alpha emitting galaxies at $z=3.1$

Jaime E. Forero-Romero¹ and Julian Mejía²

¹ *Departamento de Física, Universidad de los Andes, Cra. 1 No. 18A-10, Edificio Ip, Bogotá, Colombia*

² *Departamento de Astronomía, Universidad de Chile, Camino el Observatorio 1515, Santiago, Chile*

4 June 2013

ABSTRACT

We use cosmological N-body dark matter only simulations to constrain the characteristic mass of dark matter halos hosting Lyman-Alpha Emitting (LAE) galaxies at a redshift of $z = 3.1$. The method is based on matching the statistics for the number density between mock and observed fields. The mock fields are constructed using a simple model where a dark matter halo can only host one LAE with a probability f_{occ} if its mass is found within a certain range mass range delimited by two threshold values, M_{min} and M_{max} . We also maximize the number of mocks surveys consistent with observations and impose consistency with the angular correlation function. Under these conditions we find that LAEs are preferentially hosted by halos in very narrow mass ranges less than 0.5 dex in width, with the minimum mass $10 \leq \log_{10} M_{\text{min}} \leq 10.9$ and the occupation fraction $f_{\text{occ}} \leq 0.2$. Our finding suggest that the most massive dark matter halos at that epoch do not host the brightest LAEs. This also gives support to observational evidence that says that only a small fraction of star forming galaxies can be actually detected as LAEs.

Key words: galaxies: kinematics and dynamics, Local Group, methods:numerical

1 INTRODUCTION

Lyman- α emitting galaxies (LAEs) have become in the last decade a central topic in studies of structure formation in the Universe. They are helpful in a diverse range of fields. LAEs can be used as probes of reionization (Dijkstra et al. 2011), tracers of large scale structure (Koehler et al. 2007), signposts for low metallicity stellar populations and markers of the galaxy formation process through cosmic history (Forero-Romero et al. 2012).

At the same time, theoretical and observational developments have contributed to the emergence of a paradigm to describe structure formation in a cosmological context. In this context it is considered that dominant matter content of the Universe is to be found in dark matter, whereby each galaxy is hosted by larger dark matter structure known as a halo.

Most models of galaxy formation find that the mass of the halo can be used to predict properties of the galaxy such as its stellar mass and star formation rate (Behroozi et al. 2012). Processes that regulate the star formation cycle are also thought to be strongly dependent on its mass. Furthermore, the spatial clustering of galaxies on large scales is entirely dictated by the halo distribution. For the reasons mentioned above, finding the typical dark matter halo mass hosting LAEs represents a significant step forward to under-

stand the nature of this population in the context of Lambda Cold Dark Matter (Λ CDM) paradigm.

Some theoretical approaches to this problem have been based on a forward modeling. Starting from the DM halo population, the corresponding intrinsic star formation properties are inferred and statistics such as the luminosity function, the correlation function and the equivalent width distributions. Such modelling has been implemented from analytic considerations, semi-analytic models and full N-body hydrodynamical simulations (Dayal et al. 2009; Forero-Romero et al. 2011; Yajima et al. 2012; Forero-Romero et al. 2012).

Added to the uncertainties in the astrophysical processes describing star formation in galactic populations, a highly debated steps in this approach is the calculation of the fraction of Lyman- α photons that escape the galaxy to the observer. Given the resonance nature of the line, the radiative transfer of Lyman- α is sensitive to the density, temperature, topology and kinematics of the neutral Hydrogen in the interstellar medium (ISM) (Neufeld 1991; Forero-Romero et al. 2011; Laursen et al. 2013).

This complexity makes the use of monte-carlo simulations for the radiative transfer a required tool to obtain physically sound results, although the degeneracy in the physical parameters involved in the problem makes it difficult to achieve a robust consensus on what is the theoretical ex-

pected value for the Lyman- α escape fraction in high redshift.

Throughout this paper we assume a Λ CDM cosmology with the following values for the cosmological parameters, $\Omega_m = 0.27$, $\Omega_\Lambda = 0.73$ and $h = 0.70$, corresponding to the matter density, vacuum density and the Hubble constant in units of $100 \text{ km s}^{-1} \text{ Mpc}^{-1}$.

2 METHODOLOGY

Our method to constrain the typical mass of a dark matter halos hosting LAEs at $z = 3.1$ is based on the comparison of observational results on the surface number density and the predictions of a simple model that uses the outputs from cosmological N-body simulations.

In the next subsections we describe in detail the four key elements of this workflow. First, we present the observations we take as a benchmark. Second, the N-body simulation and the halo catalogs we use. Third, the simplified model that allows us to translated halo catalogs into mock LAE observations. Fourth, the statistics we use to compare observational results against our theoretical predictions.

2.1 Observational Constraints

The observational benchmark we use in this paper is the LAE number density information at $z = 3.1$ obtained by the panoramic narrow-band survey presented by Yamada et al. (2012) from a survey conducted with the Subaru 8.2m telescope and the Subaru Prime Focus Camera, which has a field of view covering 34×27 arcmin, corresponding to a comoving scale of $46 \times 35 \text{ Mpc } h^{-1}$ at $z = 3.09$. The narrow band filter is centered at 4977 \AA with 77 \AA width, corresponding to the redshift range $z = 3.062 - 3.125$ and $41 \text{ Mpc } h^{-1}$ comoving scale for the detection of the Lyman- α line centered at $z = 3.09$. The authors report a total 2161 LAEs with an observed equivalent width larger than 190 over a total survey area of 2.42 deg^2 , this corresponds to average surface number density of $0.20 \pm 0.01 \text{ arcmin}^{-2}$.

The survey covered four independent fields. The first is the SSA22 field of 1.38 deg^2 with 1394 detected LAEs, this field has been known to harbor a region with a large density excess of galaxies. The second observed region is composed by the fields Subaru/*XMM-Newton* Deep Survey (SXDS)-North, -Center and -South, with a total of 0.58 deg^2 and 386 LAEs. The third and fourth fields are the Subaru Deep Field (SDF) with 0.22 deg^2 and 196 LAEs, and the field around the Great Observatory Optical Deep Survey North (GOODS-N) with 0.24 deg^2 and 185 LAEs.

There is abundant observational work done on LAEs at redshift $z = 3.1$ (Kudritzki et al. 2000; Matsuda et al. 2005; Gawiser et al. 2007; Nilsson et al. 2007; Ouchi et al. 2008). However, we decide to focus on the data from Yamada et al. (2012) because it has the largest covered area with homogeneous instrumental conditions (telescope, narrow band filter), data reduction pipeline and conditions to construct the LAE catalog. This ensures that the number density variations among fields are due only to astrophysical reasons and not different observational conditions or criteria to construct the catalogs.

2.2 Simulation and Halo Catalogs

The Bolshoi simulation (Klypin et al. 2011) we use in this paper was performed in a cubic volume of $250 \text{ } h^{-1} \text{ Mpc}$ on a side. It includes dark matter distribution is sampled using 2048^3 particles, which translates into a particle mass of $m_p = 1.35 \times 10^8 \text{ } h^{-1} \text{ M}_\odot$. The cosmological parameters are consistent with a WMAP5 and WMAP7 data with a density $\Omega_m = 0.27$, cosmological $\Omega_\Lambda = 0.73$, dimensionless Hubble constant $h = 0.70$, slope of the power spectrum $n = 0.95$ and normalization of the power spectrum $\sigma_8 = 0.82$ (Komatsu et al. 2009; Jarosik et al. 2011).

We use halo catalogs constructed with a Friend-of-Friends (FOF) algorithm with a linking length of 0.17 times the interparticle distance. The minimum halo mass in the models we construct in this paper correspond to groups of ~ 75 particles. The catalogs were obtained from the publicly available Multidark database¹ (Riebe et al. 2011). We focus our work on halos more massive than $1 \times 10^{10} h^{-1} \text{ M}_\odot$ that are resolved with at least 70 particles.

2.3 A Model to Populate Halos with LAEs

In our model a dark matter halo can only host one or zero LAE. There are three parameters in the model that decide whether a halo can host a galaxy or not: the lower and upper bounds for the mass range $M_{\min} < M_h < M_{\max}$ where LAEs reside and the fraction f_{occ} of such halos that effectively host a LAE. We do not assign a luminosity to each LAE. We are primarily interested in constraining the halo mass range hosting detectable LAEs under the conditions defined by Yamada et al. (2012). In what follows will describe by the letter \mathcal{M} a model defined by an specific choice of the three scalar parameters M_{\min} , M_{\max} y f_{occ} .

For each model \mathcal{M} we create a set of mock fields from disjoint volumes in the simulation. Each volume has the same geometry probed by Suprime-CAM and the narrow band filter, namely rectangular cuboids of dimensions $46 \times 35 \times 41 \text{ } h^{-3} \text{ Mpc}^3$ where the last dimension goes in the redshift direction. This corresponds to a total area of 880 arcmin^2 in each mock field. We construct a total $5 \times 7 \times 6 = 210$ of such volumes from a snapshot in the Bolshoi simulation. In each mock field a LAE is assigned to the position of a dark matter halo if the halo mass is in the range allowed by the model $M_{\min} < M_h < M_{\max}$ and a random variable taken from an homogeneous distribution $0 \leq \xi < 1$ is smaller than the occupation fraction $\xi < f_{\text{occ}}$.

Next we construct mock surveys by making groups of 11 mock fields out of the 210 available volumes. In total 15 mock surveys are constructed for each model \mathcal{M} . The grouping is done in two different ways. In the first way, called match, we follow the clustering of the observed fields. From the 11 mock fields, 7 are constructed from contiguous fields in the simulation to mimic the SSA22 region, 3 are also contiguous between them but not to the first 7 fields to mimic the SXDS fields and finally 2 non-contiguous fields to imitate the SDF and GOODS-North field. Our main goal with this selection is to test the impact on the final statistics of having 7 clustered fields. The second way to group the

¹ <http://www.multidark.org/MultiDark/>

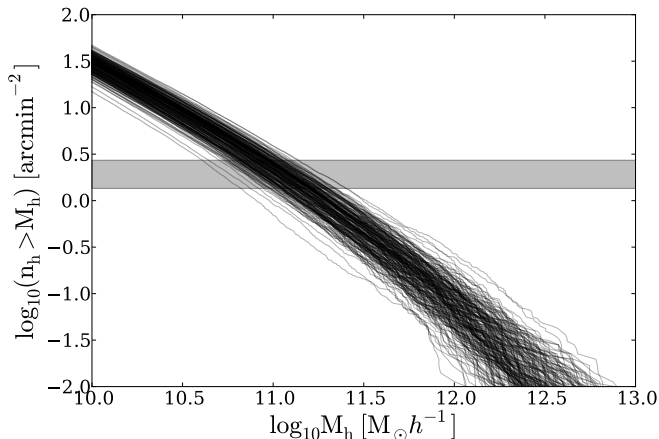


Figure 1. Surface density of dark matter halos as a function of a minimum halo mass to count the total number of elements in a volume. Each line represents one of the 210 volumes of dimensions $46 \times 35 \times 41 \text{ h}^{-3} \text{Mpc}^3$ in the Bolshoi simulation. The horizontal grey band represents the range of surface densities observed for LAEs at $z = 3.1$ as reported by (Yamada et al. 2012).

mock fields is called *random*, whereby all the 11 fields are selected in such a way as to avoid that any two volumes are contiguous.

2.4 Sampling and Selecting Models

We make a thorough exploration of the parameter space for the models \mathcal{M} . $\log_{10} M_{\min}$ takes 30 values from 10.0 up to 12.9 with an even spacing of 0.1 dex. $\log_{10} M_{\max}$ takes values in the same range as $\log_{10} M_{\min}$ only with a displacement of 0.1 dex in the whole range. The occupation fraction f_{occ} takes 10 different values from 0.1 to 1 regularly spaced by 0.1. In total the number of different models \mathcal{M} that are explored is $30 \times 30 \times 10 = 9000$.

For each mock survey generated in a given model \mathcal{M} we compute the surface density in the 12 mock fields. We perform a Kolmogorov-Smirnov (KS) to compare this mock data against the 12 observational values. From this test we obtain a value $0 < P < 1$ to reject the null hypothesis, namely that two data sets come from the same distribution. In this paper we consider that for values $P > 0.05$ the two distributions can be thought as coming from the same distribution.

In this paper we consider that a model \mathcal{M} that has at least one (1) mock survey (out of 15) consistent with the observed distribution of LAE number densities has viable parameters that deserve to be considered for further analysis.

3 BASIC RESULTS

3.1 Dark Matter Halo Number Density

In Figure 1 we present the results for the integrated dark matter halo surface density as a function of halo mass. Each line corresponds to one of the 210 sub-volumes in the Bolshoi simulation. The gray band indicates the surface density values for LAEs allowed reported in observations (Yamada et al. 2012).

This result provides the basis to understand why a range of models \mathcal{M} can be expected to be consistent with observations. In Figure 1 we can read that models with a minimum mass $\log_{10} M_{\min} > 11.5 \text{ h}^{-1} \text{M}_{\odot}$ will always have a surface number density lower than the observational constrain. The opposite is true in models with $\log_{10} M_{\min} < 10.5$ that will show surface number density larger than observations, this implies that in such models the occupation fraction has to be tuned $f_{\text{occ}} < 1.0$ as to lower the halo number density to match the gray band values.

Conversely, there are regions in the plot where the halo surface density is always higher than the observational constraints correspond to models \mathcal{M} with a minimum mass below $M_{\min} < 3 \times 10^{10} \text{ h}^{-1} \text{M}_{\odot}$. Models with this minimum mass have a chance for successfully reproducing observations if the occupation fraction $f_{\text{occ}} < 1$ is tuned as to lower the halo number density down to the observed value.

In the next subsection we quantify this intuition by means of the KS tests between mock surveys and observations.

3.2 Three Regions in Parameter Space

Figure 2 presents regions in parameter space $M_{\min} - M_{\max}$, $M_{\min} - f_{\text{occ}}$ where the KS test yields values of $P > 0.05$ at least for one mock survey. For those models it is not possible to reject the hypothesis that the simulated and observed data for the surface number density come from the same parent distribution.

The upper (lower) panels correspond to the match (random) method to build the mock surveys from individual fields. The plot shows number of mock surveys consistent with observations. There are between 550 to 600 models out of the original 9000 models that have at least one (1) mock survey consistent with observations.

In Figure ?? there are three regions of parameter space that can be clearly distinguished. The first region corresponds to models where the minimum mass is high $\log_{10} M_{\min} > 11.5$. None of these models is compatible with observations as expected from the results in the previous section. For these models the number density of LAEs is too low.

The second region corresponds to an intermediate range for the minimum mass $10.5 < \log_{10} M_{\min} < 11.5$ where regardless of the value of the maximum mass M_{\max} it is possible to tune the occupation fraction f_{occ} to bring some of the mock observations into good agreement with observations. In this region in parameter space one can thus find two extreme kinds of models. One kind where the mass interval is very narrow with sizes smaller than < 0.3 dex (a factor of two in mass) and others where the mass interval is very extended, larger than 1.0 dex, going up to the maximum halo mass present in the simulation at that redshift.

The third region in parameter space corresponds to $\log_{10} M_{\min} < 10.5$. In this case only models with a narrow mass interval of at most 0.5 dex ($\log_{10} M_{\max} < 11.0$) and low occupation fractions $f_{\text{occ}} < 0.3$ are allowed.

Without any additional information our method allows us to infer that most of the successful models are found in the second and third region of parameter space where. This result was already expected from halo abundance calculations shown in Figure 1. In the next section we reduce the size of this region by using more stringent constraints to define the



Figure 2. M_{\min} - M_{\max} (left) and $M_{\min} - f_{\text{occ}}$ (right) planes for all models with $P > 0.05$ in two different ways used to construct the mock surveys. The color code corresponds to the number of mock surveys that are found to be compatible with observations in terms of the KS test with $P > 0.05$. Only regions of parameter space with at least one (1) consistent mock survey are included.

agreement with observations and including additional observational information on possible values for the occupation fraction at $z \sim 3$.

4 ADDITIONAL CONSTRAINTS

In this section we consider three additional constraints on the models we accept as successful. First by taking models with the highest possible number of mock surveys consistent with observations. Second by including additional observational constraints on the occupation fraction for high redshift LAEs. Third by comparing the angular correlation function against observational constraints by Hu et al. (2004).

4.1 Models with the highest success rates

For each model \mathcal{M} there are 15 different mock surveys. In the previous section we presented the models that had at least one (1) mock survey with $P > 0.05$.

Figure 3 shows the number of models that have at least $N_{\text{high-P}}$ mocks with $P > 0.05$ for the match and random methods. This shows that there are here between 80 to 100 models with all the 15 realizations with $P > 0.05$. This is a reduction of a factor of ~ 6 with respect to the total number of mocks with at least one consistent mock.

Figure 4 presents the loci of these models in the parameter space $M_{\min} - M_{\max}$ and $M_{\min} - f_{\text{occ}}$ for the match method, the results for the random method are similar. In this case the models with $\log_{10} M_{\min} < 11.7$ are greatly reduced. This corresponds to the regions in the parameter space in Figure 2 that already had a low number of consistent mock surveys. From the right panel in Figure 4 one

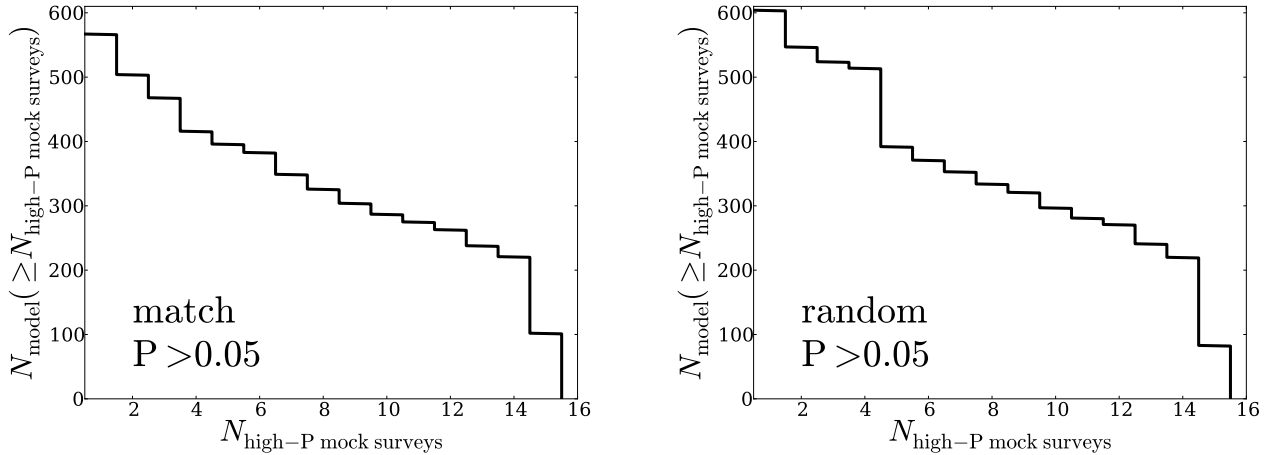


Figure 3. Number of models with a minimum number of mock survey realizations that are consistent with observations. .

can see that there is not a strong selection effect on the occupation fraction f_{occ} .

4.2 Additional Constraints on the Occupation Fraction

We impose an additional restriction using the observational results by Hayes et al. (2010). They constrained the value of f_{occ} at $z = 2.2$ to be $f_{\text{occ}} = 0.10$. This estimation was based on blind surveys of the $\text{H}\alpha$ and Lyman α line with the European Southern Observatory (ESO) Very Large Telescope (VLT). Using corrections by extinction to obtain an estimate for the intrinsic $\text{H}\alpha$ luminosity, and using values for the theoretical expectation of the ratio Lyman α / $\text{H}\alpha$ they derive a bulk escape fraction for the Lyman α radiation of $f_{\text{esc}} = (5.3 \pm 3.8)\%$ or $f_{\text{esc}} = (10.7 \pm 2.8)\%$ if a different dust correction is used. The authors show that the luminosity function for LAEs at $z = 2.2$ is consistent with the escape fraction being constant for every galaxy regardless of its luminosity. From this results they derive that almost 90% of the star forming galaxies emit insufficient Lyman α to be detected, effectively setting the occupation fraction to be $f_{\text{occ}} = 0.10$. For the cosmological parameters used in this paper the age of the universe between $z = 3.1$ and $z = 2.2$ has changed by ~ 1 Gyr. We assume that the physical conditions that determine the escape fraction f_{esc} and the occupation fraction f_{occ} remain similar over that time scale.

We limit the occupation fraction to be in the range $f_{\text{occ}} \leq 0.2$ to allow for some flexibility on the time evolution and the uncertainty in the dust correction used to infer the escape fraction. Figure 5 shows the preferred models in the planes $M_{\text{min}} - M_{\text{max}}$ and $M_{\text{min}} - f_{\text{occ}}$ for the **match** and **random** methods. With this additional constraint between 35 to 40 models are consistent with observations, this represents a factor of ~ 2 reduction. All the models with $\log_{10} M_{\text{min}} \geq 11.0$ are now excluded and the best models are now clustered around a narrow region in parameter space.

4.3 Consistency with the Angular Correlation Function

The measurements presented in (Yamada et al. 2012) do not present a new measurement of the angular correlation function (ACF). However (Hu et al. 2004) performed such calculation on the LAEs observed in the densest field of SSA22.

We calculate the angular correlation function (ACF) for all the models having the 15 mock surveys consistent with observations. We perform this calculation as a sanity check and potential additional constraint. The ACF is computed only the densest subfield in all the 15 mock surveys corresponding to the SSA22 region.

It is important to keep in mind that there are some differences between this work and (Yamada et al. 2012). The color selection by Yamada et al. (2012) is less stringent compared to the one by Hu et al. (2004). Also the EW threshold is different, Hu et al. (2004) uses a cut around 154\AA instead of 190\AA used by (Yamada et al. 2012).

The comparison between the simulated and observed ACFs is also done using a χ^2 statistic which includes the information on the measurement uncertainties and the statistical dispersion from the 15 mock surveys in the simulation

$$\chi^2 = \sum_{\theta_i} \frac{(\xi_{\text{obs}}(\theta_i) - \xi_{\text{sim}}(\theta_i))^2}{\sigma_{\text{obs}}^2(\theta_i) + \sigma_{\text{sim}}^2(\theta_i)}, \quad (1)$$

where the sum is done over all the 13 angle values θ_i where the ACF has been computed. In Figure XX we plot this statistic for all the models considered. In all cases $\chi^2 < 7$ which is not sufficient to consider that the correlation functions from the simulations are statistically different from the observational one. The contribution of cosmic variance in the simulations together with the statistical uncertainties make all tested models compatible with the observational constraints.

We also present the results for the mean angular correlation function in terms of the angular correlation length obtained by fitting to a power-law function:

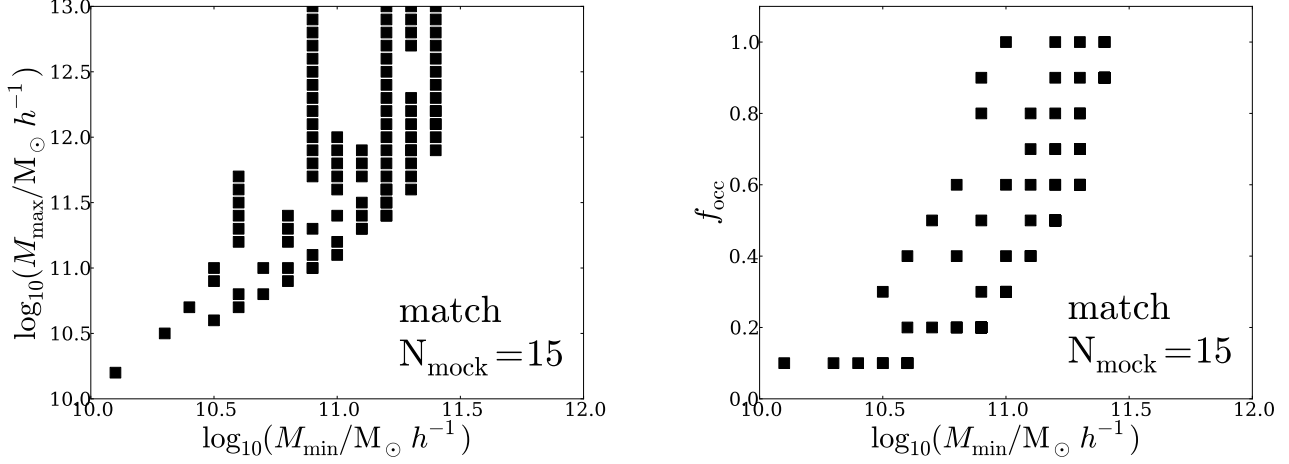


Figure 4. Favored regions in parameter space when the constraints on the maximal number of consistent mocks is imposed. The results for the random methodology (not shown here) are very similar to the ones presented here for the match method.

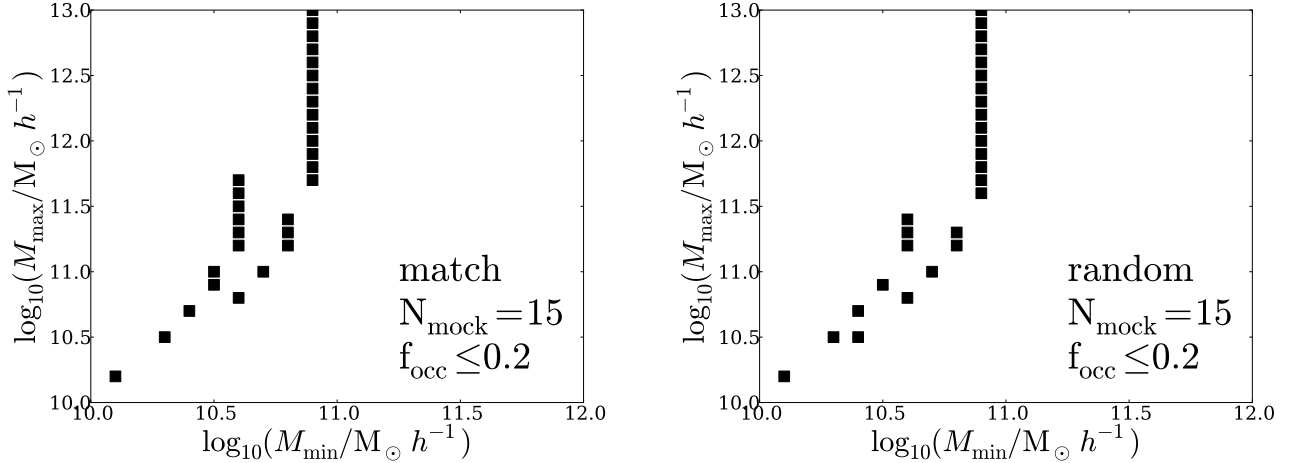


Figure 5. Best models when both the constraints on the maximal number of consistent mocks and the occupation fraction $f_{\text{occ}} \leq 0.2$ are included.

$$\xi(\theta) = \left(\frac{r}{\theta_0} \right)^{-\gamma} \quad (2)$$

The fitting is done to both the mean ACF and the observational ACF reported by Hu et al. (2004). The results are shown in Figure 6 in a $\theta_0 - \gamma$ plane where the average and standard deviation for each mock are shown in comparison with the result derived from observations. Error bars in these figures represents the standard deviation of the ACF over all the sub-fields.

It can be seen in the left panel figure 6 that The observational ACF measured by Hu et al. (2004) (green dot) set additional constrains on the parameters models. Only models with angular-correlation lenght within $\theta_0 \sim [15, 23] \text{arcsec}$ reproduces observations and this rule out several models.

In order to identify the models that are consistent with observation we plot if the right panel of figure 6 θ_0 vs M_{min} and divide the plots into two sets: Those models

with $\log \frac{M_{\text{max}}}{M_{\odot}} < 12$ (blue dots) and those with $\log \frac{M_{\text{max}}}{M_{\odot}} > 12$ (green dots). The red rectangle includes the parameter region wich is consistent with the observational constraint in θ_0 . With this restriction we find that models with $\log \frac{M_{\text{max}}}{M_{\odot}} > 12$ and $\log \frac{M_{\text{min}}}{M_{\odot}} > 11.1$ can be ruled out.

Finally, we also present the ACF in the case of the full SSA22 region which has been homogeneously observed by (Yamada et al. 2012). To this date the observational ACF has not been reported in the literature, therefore our calculations can be considered as predictions.

In Figure X we present the results for the models. The full list of these correlation functions can be found in the the data repository for this paper in [github](#).

5 DISCUSSION

When we include the tightest constraints on the mock catalogs, we find that there are 30 set of parameters of our model,

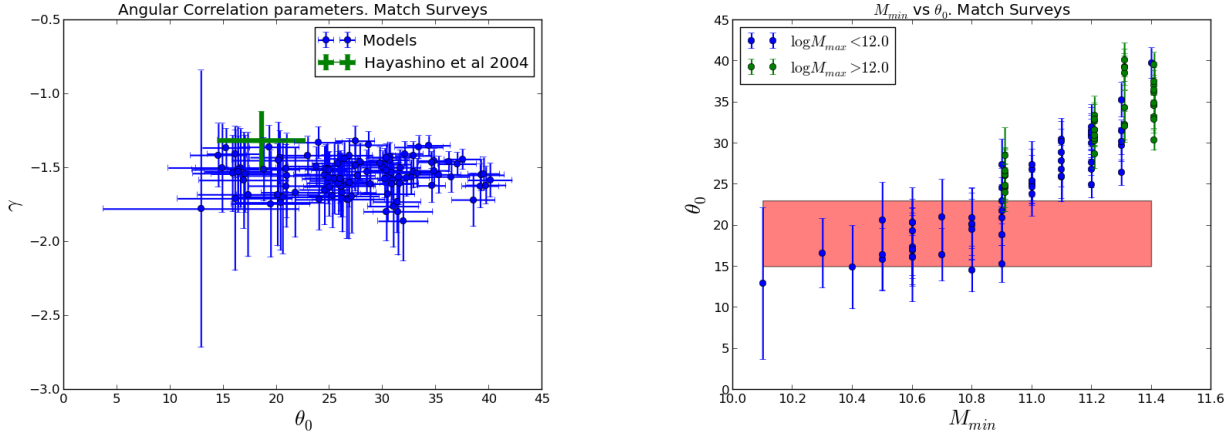


Figure 6. Left: The fitted parameters (θ_0 vs γ) of the mean ACF assuming a powerlaw behavior. Each blue dot corresponds to a match-model while the green dot represent the powerlaw fit of the observational ACF reported by Hu et al. (2004). The error bars represents the dispersion in each parameter over all the mock surveys for a given model and dispersion due to the observational error for the measured ACF by Hu et al. (2004). Right: θ_0 vs M_{min} . The data is subdivided into two blocks $M_{max} < 12.0$ (blue) and $M_{max} > 12.0$ (green). The red rectangle includes the region within models are consistent with the observational angular-correlation length ($15 < \theta_0 < 23$) as it can be deduced from the left panel.

out of the original 90000 initial models, that are consistent with the observational constraints at redshift 3.1: the distribution of the number density, the inferred values for the average occupation fraction. The consistency with the angular correlation, in terms of the χ^2 statistics did not help to discard any additional models with a significant degree of confidence.

These 30 models can be classified into two families of the same size. The first, where the range $M_{min} - M_{max}$ is narrow, typically of less than < 1.0 dex. While in the second family the extent > 1.0 dex. In the first case the minimum halo mass is found to be in a wide range $10^{10} h^{-1} M_{\odot} < M_{min} < 10^{11.5} h^{-1} M_{\odot}$ while in the second case, only models with $M_{min} \sim 10^{10.9} h^{-1} M_{\odot}$ are compatible with the observational constraints. In what follows we discuss the implications of the existence of these two families of models.

When we additionally include the ACF constraint we find that only models with $\log_{10} M_{min} \leq 11.0$ and $\log_{10} M_{max} \leq 12.0$ are now consistent with observations.

Including all the observational constraints we find that only between 15 to 20 models reproduce observations. The list for the model parameters is in the Appendix in Table 1.

5.1 Implications for galaxy formation models

In the case of a narrow range of masses to host LAEs the upper masses are bound to be $M_{max} < 10^{11.5} h^{-1} M_{\odot}$ as it is shown in Figure ?? . For halos more massive than this bound it is naturally expected that the galaxies can be observed as Lyman Break Galaxies (LBGs). This would imply that not all the bright LBGs can be detected as a LAE.

We have the opposite situation in the second family of models. If we have a wide range in halo masses, where the upper end of the halo masses can be considered as observed LAEs, one can expect that bright LBGs will have a correspondence as observed LAEs. The most interesting aspect is that there is a clear cut in the minimal mass that can be

attained by observed LAEs $M_{min} > 10^{11} h^{-1} M_{\odot}$. This puts a tight constraint on the relationship between the minimum star formation rate required to be observed as a LAE and this minimal halo mass.

- ... Intrinsic emission and escape fraction.
- ... Star formation rate efficiency at this redshift.
- ... Mass dependence of the escape fraction.
- ... Discuss all this in terms of the star formation efficiency in Behroozi et al.

5.2 Implications for large LAEs surveys

- ... The bias for the preferred halo mass.
- ... The scale at which cosmic variance drops.
- ... This can be observationally tested with HETDEX.

5.3 On the reproducibility of our results

- ... All the software to produce the results in this paper is publicly available.
- ... The raw catalogs can be obtained from the MultiDark database but can also be obtained in the repository of this paper on github.

6 CONCLUSIONS

In this paper we constrain the preferred mass for dark matter halos hosting Lyman Alpha Emitters at a redshift $z = 3.1$. We use a method that matches the cosmic variance in the surface density number of LAEs between mock and real observations. The mock catalogs are based on a simplified model with three basic parameters: the halo mass range where LAEs can be found, $M_{min} < M_h < M_{max}$, and the fraction of the halos in this range that are actually occupied, f_{occ} . After a thorough exploration of the parameter space we are able to constrain the mass range of dark matter halos

$\log_{10} M_{\min}$	$\log_{10} M_{\max}$	f_{occ}
10.1	10.2	0.1
10.3	10.5	0.1
10.4	10.7	0.1
10.5	10.9	0.1
10.5	11.0	0.1
10.6	11.2	0.1
10.6	11.3	0.1
10.6	11.4	0.1
10.6	11.5	0.1
10.6	11.6	0.1
10.6	11.7	0.1
10.6	10.8	0.2
10.7	11.0	0.2
10.8	11.2	0.2
10.8	11.3	0.2
10.8	11.4	0.2
10.9	11.7	0.2
10.9	11.8	0.2
10.9	11.9	0.2

Table 1. List of model parameters for the best models that have all mock surveys consistent with observations and an occupation fraction $f_{\text{occ}} \leq 0.2$. This corresponds to the match method to construct the mock surveys. .

hosting LAEs to be in the range $< M_h <$ and a corresponding occupation fraction that scales as $f_{\text{occ}} = M_{\min}$.

We use three additional constraints to reduce the allowed range of models. The first imposes a tighter criterion to consider a model successful, namely that all the mock surveys for a given model must be consistent with observations. This restriction narrows down the allowed range of models to be.

The second constraint is based on the observational results that high redshift LAEs have a bulk Lyman alpha escape fraction of XX which can be also interpreted as an average occupation fraction of XX .

Including additional observational constraints on the occupation fraction allows us to reduce the range of allowed halo masses to be in a narrower range of $< M_h <$. Including the information from the angular correlation function (ACF) does not allow us to impose further constraints. This is due to the scatter in the ACF due to the cosmic variance on the field observed by XXX .

We simulation allows us to extract 210 sub-boxes each of which has a comparable volume to the individual fields of view observed by Yamada et al. (2012). The comparison of the observed number density distribution against the results from our model is based on three different ways of constructing mock surveys. The first reproduces the spatial correlation between the 12 observational fields (match), the second breaks this spatial correlation while keeping the number of fields (random) and the third one simply includes all the 210 sub-boxes (full). We find that the methods match and random allow a larger set of models than the random method. We do not find a significant difference between the two first methods.

ACKNOWLEDGMENTS

REFERENCES

- Behroozi P. S., Wechsler R. H., Conroy C., 2012, ArXiv e-prints
- Dayal P., Ferrara A., Saro A., Salvaterra R., Borgani S., Tornatore L., 2009, MNRAS, 400, 2000
- Dijkstra M., Mesinger A., Wyithe J. S. B., 2011, MNRAS, 414, 2139
- Forero-Romero J. E., Yepes G., Gottlöber S., Knollmann S. R., Cuesta A. J., Prada F., 2011, MNRAS, 415, 3666
- Forero-Romero J. E., Yepes G., Gottlöber S., Prada F., 2012, MNRAS, 419, 952
- Gawiser E., Francke H., Lai K., Schawinski K., Gronwall C., Ciardullo R., Quadri R., Orsi A., Barrientos L. F., Blanc G. A., Fazio G., Feldmeier J. J., 2007, ApJ, 671, 278
- Hayes M., Östlin G., Schaerer D., Mas-Hesse J. M., Leitherer C., Atek H., Kunth D., Verhamme A., de Barros S., Melinder J., 2010, Nature, 464, 562
- Hu E. M., Cowie L. L., Capak P., McMahon R. G., Hayashino T., Komiyama Y., 2004, AJ, 127, 563
- Jarosik N., Bennett C. L., Dunkley J., Gold B., Greason M. R., Halpern M., Hill R. S., Hinshaw G., Kogut A., Komatsu E., Larson D., Limon M., 2011, ApJS, 192, 14
- Klypin A. A., Trujillo-Gomez S., Primack J., 2011, ApJ, 740, 102
- Koehler R. S., Schuecker P., Gebhardt K., 2007, A&A, 462, 7
- Komatsu E., Dunkley J., Nolte M. R., Bennett C. L., Gold B., Hinshaw G., Jarosik N., Larson D., Limon M., Page L., Spergel D. N., Halpern M., 2009, ApJS, 180, 330
- Kudritzki R.-P., Méndez R. H., Feldmeier J. J., Ciardullo R., Jacoby G. H., Freeman K. C., Arnaboldi M., Capaccioli M., Gerhard O., Ford H. C., 2000, ApJ, 536, 19
- Laursen P., Duval F., Östlin G., 2013, ApJ, 766, 124
- Matsuda Y., Yamada T., Hayashino T., Tamura H., Yamauchi R., Murayama T., Nagao T., Ohta K., Okamura S., Ouchi M., Shimasaku K., Shioya Y., Taniguchi Y., 2005, ApJL, 634, L125
- Neufeld D. A., 1991, ApJL, 370, L85
- Nilsson K. K., Møller P., Möller O., Fynbo J. P. U., Michałowski M. J., Watson D., Ledoux C., Rosati P., Pedersen K., Grove L. F., 2007, A&A, 471, 71
- Ouchi M., Shimasaku K., Akiyama M., Simpson C., Saito T., Ueda Y., Furusawa H., Sekiguchi K., Yamada T., Kodama T., Kashikawa N., Okamura S., Iye M., Takata T., Yoshida M., Yoshida M., 2008, ApJS, 176, 301
- Riebe K., Partl A. M., Enke H., Forero-Romero J., Gottlöber S., Klypin A., Lemson G., Prada F., Primack J. R., Steinmetz M., Turchaninov V., 2011, ArXiv e-prints
- Yajima H., Choi J.-H., Nagamine K., 2012, MNRAS, 427, 2889
- Yamada T., Nakamura Y., Matsuda Y., Hayashino T., Yamauchi R., Morimoto N., Kousai K., Umemura M., 2012, AJ, 143, 79